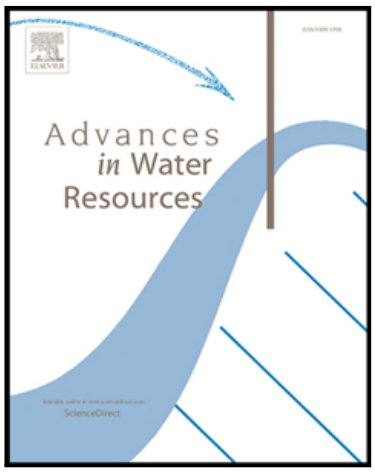

Capillary filling and Haines jump dynamics using free energy Lattice Boltzmann simulations

Ioannis Zacharoudiou, Edo S. Boek

PII: S0309-1708(16)30077-X
DOI: 10.1016/j.advwatres.2016.03.013
Reference: ADWR 2580

To appear in: *Advances in Water Resources*

Received date: 16 July 2015
Revised date: 21 March 2016
Accepted date: 25 March 2016

Please cite this article as: Ioannis Zacharoudiou, Edo S. Boek, Capillary filling and Haines jump dynamics using free energy Lattice Boltzmann simulations, *Advances in Water Resources* (2016), doi: 10.1016/j.advwatres.2016.03.013

Highlights

- Capillary filling
  a. Correct dynamics in the limit of large times for high and low viscosity ratios (1. scaling of length with time and 2. variation of the dynamic contact angle)
  b. Correct dynamics in the limit of small times (two successive regimes of length vs time precede the Lucas-Washburn regime)
- Haines jump events
  a. Associated with both drainage and capillary filling dynamics
  b. Non-local, cooperative events with imbibition occurring during drainage of a pore body in the surrounding pore throats. This leads to fluid redistribution in the area of the surrounding draining pore.
  c. Role of the Ohnesorge number in determining draining times.
  d. Role of the Ohnesorge number in identifying the type of pore filling dynamics that will occur.

Capillary filling and Haines jump dynamics using free energy Lattice Boltzmann simulations

Ioannis Zacharoudiou[a,*], Edo S. Boek[a,b]

[a] *Department of Chemical Engineering, Imperial College London, South Kensington Campus, London SW7 2AZ, United Kingdom*
[b] *Department of Chemistry, University of Cambridge, Lensfield Road, Cambridge CB2 1EW, United Kingdom*

Abstract

We investigate numerically the dynamics of capillary filling and Haines jump events using free energy Lattice Boltzmann (LB) simulations. Both processes are potentially important multi-phase pore-scale flow processes for geological CO_2 sequestration and oil recovery. We first focus on capillary filling and demonstrate that the numerical method can capture the correct dynamics in the limit of long times for both high and low viscosity ratios, i.e. the method gives the correct scaling for the length of the penetrating fluid column as a function of time. Examining further the early times of capillary filling, three consecutive *length* vs. *time* regimes have been observed, in agreement with available experimental work in the literature. In addition, we carry out simulations of Haines jump events in idealised and realistic rock pore geometries. We observe that the Haines jump events are cooperative, non-local and associated with both drainage and imbibition dynamics. Our observations show that the pore filling dynamics is controlled by the Ohnesorge number, associated with the balance between viscous forces and inertial / surface tension forces. Using this concept, we are able to identify the type of pore filling dynamics that will occur.

Keywords: Capillary filling, Haines jump events, interfacial jumps, pore scale modeling, drainage, free energy Lattice Boltzmann method

*Corresponding author
Email address: i.zacharoudiou@imperial.ac.uk (Ioannis Zacharoudiou)

1. Introduction

Our understanding for multiphase flow, which is extremely important for many industrial, environmental and biological applications, can be greatly enhanced by numerical modeling. As exact solutions to the equations of motion are not an easy task or in most of the cases impossible to obtain, modeling multiphase flow can provide invaluable insights, but more importantly can be a useful predictive tool. In porous media the coupling of the flow, the fluid-fluid interface displacement and the interactions with the solid surfaces and the complex geometry adds to the complexity of investigating multiphase systems.

Macroscopic mathematical models developed, based on solving generalisations of Darcy's law, neglect non-equilibrium and inertial effects since the flow is at small Reynolds numbers. These models are based on the fundamental assumption of local phase equilibrium [1, 2, 3], which is valid when the characteristic time-scale of a process is much larger than the time for redistribution of the fluids along their flow paths occurring in multiphase flow due to changes in capillary pressure [4]. Non-equilibrium effects become, however, important when the above time-scales are comparable in size [4]. This applies to processes such as (a) CO_2 displacing water (drainage) in geological CO_2 sequestration and (b) water displacing oil (forced imbibition) in oil recovery, where pore scale instabilities can cause an abrupt increase in the interfacial velocity decreasing the characteristic transition time. Haines jump events, a characteristic feature of two-phase flows in porous media at the pore scale, are an example of the former [5, 6, 7, 8]. Although first discovered more than 80 years ago [9], it was only recently that advances in synchrotron micro-CT enabled the direct observation of such events in porous media flow in real time[5]. For the latter, Ferrari and Lunati [10] demonstrated numerically that inertial effects induce interfacial oscillations that can influence the selection of the next pore to be invaded and hence the displacement pathways. Therefore, in these situations solving the full Navier-Stokes equations at the pore scale is necessary to resolve the correct fluid displacement flow paths [10, 8].

Here we use the free energy Lattice Boltzmann (LB) method [11, 12] to investigate drainage and in particular the dynamics of Haines jump events, in light of recent experimental observations[5, 6] demonstrating that these abrupt events are associated with both drainage and imbibition dynamics. Hence, we first examine capillary filling dynamics and the time-scales involved, before turning our attention to Haines jump events.

The phenomenon of imbibition or capillary filling has been extensively studied during the last century. A fluid penetrates a hydrophilic channel under the action of capillary filling, due to the Laplace pressure across the interface, or equivalently due to the decrease in the free energy of the system as the liquid wets the walls of the channel. The system uses the energy liberated from wetting the walls to drive the fluid inside the capillary. A renewed interest in the subject is due to modern applications of microfluidic devices. Developments in lithographic techniques and the ability to fabricate microchannels on micron length scales lead to a plethora of applications where the phenomenon of capillary filling can be exploited to achieve the desired outcome; from entropic traps for DNA separation [13], chemical detection [14], as microreactors [15] and one way flow microchannels achieved via surface patterning.

Lucas [16] and Washburn [17] gave the first account of the phenomenon, but considered only the regime when all influences apart from the driving force, the capillary force, and the viscous drag cease to exist. Still their predictions could describe the experimentally observed time dependency of the filled length of the penetrating fluid, which is that the length of the fluid column is proportional to the square root of time, $l \sim t^{0.5}$. Several authors have further progressed the subject by considering effects not taken into account by Lucas and Washburn, like inertial [18, 19] and gravitational effects [20], deviations from a Poisseuile velocity profile at the inlet of the capillary or at the interface [21, 19, 22] and variations of the dynamic contact angle [18, 23]. Work also extended to rough capillaries [24] and patterned channels [25, 26]. Moreover, extensive work in the literature involved the initial stages of capillary filling, as the Lucas-Washburn regime is the asymptotic limit for large times [27, 28, 29, 18, 30, 31].

Capillary filling plays a potentially important role in geological CO_2 sequestration, as it occurs in both stages of the process. Following the initial stage of drainage and once the injection of CO_2 stops, brine, as the wetting phase, reenters the pore matrix due to the action of capillary filling. This traps CO_2 and determines eventually the amount of CO_2 that is stored in the pore space. Maybe not so evident, capillary filling can occur during the first injection phase as well, as it can be associated with Haines jump events [6, 7].

We will now give a brief overview of different approaches for pore scale flow simulations. Pore-network models [32, 33] have been developed to understand multiphase flows at the pore scale. These models are simplified representations of the real pore space and therefore computationally efficient. However, the simplifications imposed often restricts their predictive capability and accuracy. Traditional Computational Fluid Dynamics (CFD) methods include the volume-of-fluid (VOF) [34, 35, 36] and level set (LS) approaches [37, 38]. These methods are able to simulate multiphase flows by explicitly solving the macroscopic Navier-Stokes equations. In addition, these approaches require a method to track the fluid-fluid interface. Together, this poses a considerable computational challenge for both VOF and LS when the computational domain is significant. In addition, using classical CFD approaches, it is difficult to incorporate fluid-solid interfacial effects such as surface wettability.

Here we consider the LB method [39, 40, 41, 42] as a numerical algorithm alternative to conventional CFD methods. LB solves the discrete Boltzmann equation, and reproduces the Navier-Stokes equations in the continuum limit. It is becoming increasingly popular in several fields of computational fluid dynamic engineering, mainly because of its efficiency and simplicity in terms of implementation, while it is particularly well suited for computations on a parallel architecture. We take advantage of this and exploit the opportunities offered by high performance hardware like General Purpose Graphics Processing Units (GPGPUs).

The free energy LB method is a thermodynamically consistent extension of the LB method developed in the Yeomans' group [11, 12]. The method con-

stitutes a mesoscale approach [43], because it has the ability to exploit the underlying microscopic structure of the equations of motion, without resorting to a description of the fluid in terms of molecular dynamics [44]. This gives the advantage to easily incorporate complex physical phenomena in the algorithm, ranging from phase behavior, multiphase flows to chemical interactions between the fluid and the surrounding solid surfaces. Moreover, it avoids the need to track the time evolution of the interface between different phases [45], which makes it ideal to study problems involving the time evolution of fluid-fluid interfaces [46, 47].

It is worth pointing out that a recent alternative Navier-Stokes solver, called Direct Hydrodynamics (DHD) also adopts a Cahn-Hilliard description of the free energy [48]. However, the dynamics of the system is solved using a Density Functional Theory approach, which is distinctly different from the LB method used in this paper.

Our aim in this paper is to demonstrate that the numerical approach we choose, the free energy Lattice Boltzmann method, can be used to effectively solve the hydrodynamic equations of motion and investigate problems related to multiphase flow at the pore scale. With regards to capillary filling dynamics, the method captures the correct physics of capillary filling, both in the limit of large and small time-scales. The dynamical testing involves the scaling of the imbibition length with time, as well as the time variation of the dynamic contact angle and its dependency on the interface velocity. Then, we demonstrate how Haines jump events, associated with a drainage situation, are coupled with imbibition dynamics. Correctly capturing the dynamics of these transient events, that involve both drainage and spontaneous imbibition dynamics, ensures that the fluid spatial redistribution occuring during these events will be correctly resolved.

The paper is organised as follows. In Section 2 we briefly present the details of the numerical method we choose to solve the governing equations for a system of a binary fluid, which include both the thermodynamics and hydrodynamics of the system. Section 3 is devoted to capillary filling, while in Section 4 we

turn our attention to the Haines jumps problem. Finally, conclusions from this work are drawn in Section 5.

2. Numerical Model

The free energy LB method belongs to a class of hydrodynamic models, called diffuse interface models [49, 50, 51, 52], where the fluid-fluid interface has a finite thickness. Far away from a contact line, the method solves the hydrodynamic equations of motion of the fluid, i.e. the Navier-Stokes equations and the continuity equation. In the vicinity of the contact line, however, due to the finite thickness of the interface, the method introduces a diffusive mechanism, which regularizes the viscous dissipation singularity [53] and allows the contact line to slip on a solid substrate.

2.1. Thermodynamics of the fluid

The equilibrium properties of a binary (two-phase) fluid can be described by a Landau free energy functional [52]

$$\mathcal{F} = \int_V \left(f_b + \frac{\kappa_\phi}{2} (\partial_\alpha \phi)^2 \right) dV + \int_S f_s \, dS \, . \tag{1}$$

The first term in the integrand is the bulk free energy density given by

$$f_b = \frac{A}{2}\phi^2 + \frac{B}{4}\phi^4 + \frac{c^2}{3}\rho \ln \rho \, , \tag{2}$$

where ϕ is the concentration or order parameter, ρ is the fluid mass density and c is a lattice velocity parameter. This choice of f_b allows binary phase separation into two phases if $A < 0$ and $B > 0$, as the bulk free energy density takes the form of a double-well potential, with bulk equilibrium solutions $\phi_{eq} = \pm(-A/B)^{1/2}$. Here we make the choice $A = -B$, which leads to $\phi_{eq} = \pm 1$ for the two phases. The position of the interface is chosen to be at $\phi = 0$. The final term in the bulk free energy density, $\frac{c^2}{3}\rho \ln \rho$, does not affect the phase behavior and is added to enforce incompressibility [54].

The gradient term $\frac{\kappa_\phi}{2}(\partial_\alpha \phi)^2$ in eq. 1 penalizes spatial variations of the order parameter ϕ, for example across an interface, and ensures a smooth transition

from one phase to the other; hence, this term is related to the interface tension $\gamma = \sqrt{-8\kappa_\phi A^3/9B^2}$ and to the interface width $\xi = \sqrt{-\kappa_\phi/A}$ [52].

The final term in the free energy functional, eq. 1, describes the interactions between the fluid and the solid surface. Following [55], the surface energy density is taken to be of the form $f_s = -h\phi_s$, where ϕ_s is the value of the order parameter at the surface. Minimisation of the free energy gives an equilibrium wetting boundary condition [52]

$$\kappa_\phi \, \partial_\perp \phi = -\frac{df_s}{d\phi_s} = -h \; . \tag{3}$$

The value of the parameter h (the surface excess chemical potential) is related to the equilibrium contact angle θ^{eq} via [52]

$$h = \sqrt{2\kappa_\phi B}\, \mathrm{sign}\left[\frac{\pi}{2} - \theta^{\mathrm{eq}}\right] \sqrt{\cos\left(\frac{\alpha}{3}\right)\left\{1 - \cos\left(\frac{\alpha}{3}\right)\right\}} \; , \tag{4}$$

where $\alpha = \arccos\left(\sin^2\theta^{eq}\right)$ and the function sign returns the sign of its argument.

This choice of the free energy leads to the (exchange) chemical potential

$$\mu = \frac{\delta \mathcal{F}}{\delta \phi} = A\phi + B\phi^3 - \kappa_\phi \partial_{\gamma\gamma}\phi \; , \tag{5}$$

which describes the change in $\mathcal{F}$ for a small change in concentration, and is constant in equilibrium. The pressure tensor, which determines how the system approaches equilibrium, is given by [56, 54]

$$\begin{aligned} P_{\alpha\beta} &= \left[\phi\frac{\delta\mathcal{F}}{\delta\phi} + \rho\frac{\delta\mathcal{F}}{\delta\rho} - \mathcal{F}\right]\delta_{\alpha\beta} + (\partial_\alpha\phi)\frac{\delta\mathcal{F}}{\delta(\partial_\beta\phi)} \\ &= \left[p_b - \kappa_\phi\phi\partial_{\gamma\gamma}\phi - \frac{\kappa_\phi}{2}(\partial_\gamma\phi)^2\right]\delta_{\alpha\beta} + \kappa_\phi(\partial_\alpha\phi)(\partial_\beta\phi) \\ &= P^{iso}\delta_{\alpha\beta} + P^{chem}_{\alpha\beta} \; , \end{aligned} \tag{6}$$

where $p_b = \frac{c^2}{3}\rho + \frac{1}{2}A\phi^2 + \frac{3}{4}B\phi^4$ is the bulk pressure. The pressure tensor comprises of two terms, a 'chemical' pressure tensor contribution $P^{chem}_{\alpha\beta}$ and an isotropic contribution $P^{iso} = \frac{c^2}{3}\rho$ to ensure constant density [54]. $P^{chem}_{\alpha\beta}$ originates from the fact that, in the presence of concentration gradients, there is a thermodynamic force density $-\phi(\partial_\alpha\mu)$ acting at each point of the fluid, which

can be expressed as the divergence of a 'chemical' pressure tensor $\phi(\partial_\alpha \mu) = \partial_\beta P^{chem}_{\alpha\beta}$. Effectively this thermodynamic force density pulls the two fluids in opposite directions due to the chemical potential gradient, with the net force being zero at the interface ($\phi = 0$).

For a free energy based multicomponent LB method we refer the reader to [57, 58].

2.2. Equations of motion

The hydrodynamic equations for the system are the continuity, eq. 7, and the Navier-Stokes, eq. 8, equations for a nonideal fluid

$$\partial_t \rho + \partial_\alpha(\rho u_\alpha) = 0 \,, \tag{7}$$

$$\partial_t(\rho u_\alpha) + \partial_\beta(\rho u_\alpha u_\beta) = -\partial_\beta P_{\alpha\beta} + \partial_\beta \left[\eta(\partial_\beta u_\alpha + \partial_\alpha u_\beta)\right] + F_\alpha \,, \tag{8}$$

where $\mathbf{u}$, $\mathbf{P}$, η, $\mathbf{F} = \rho\mathbf{g}$ are the fluid velocity, pressure tensor, dynamic viscosity and body force respectively. For a binary fluid the equations of motion are coupled with a convection-diffusion equation,

$$\partial_t \phi + \partial_\alpha(\phi u_\alpha) = M\nabla^2 \mu \,, \tag{9}$$

that describes the dynamics of the order parameter ϕ. M is a mobility coefficient.

The above equations are solved using a Multiple Relaxation Time (MRT) Lattice Boltzmann algorithm [59]. Details of the implementation of the Lattice Boltzmann algorithm are given in the references [52, 45, 23] and are not repeated here. An important remark here is that the continuity and Navier Stokes equations are coupled to an advection-diffusion equation and are not solved independently. This ensures that the equations are solved with an algorithm that is consistent with the thermodynamics of the fluids, which enters the equations of motion through the chemical potential and pressure tensor. The coupling occurs at the level of the distribution functions, as the concentration and its spatial gradients appear in the equilibrium distribution functions for

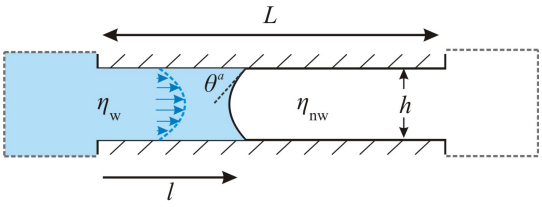

Figure 1: Schematic representation of the simulation geometry.

the density and in the Pressure tensor (see [52, 45, 23] for more details). The evolution of the order parameter (concentration) is obtained from solving the advection-diffusion equation. The order parameter responds to the flow (velocity field obtained from solving Navier Stokes and continuity), as it can be advected by the flow, but also responds to chemical potential gradients. This evolution of the concentration field results in a change of the pressure field which in turn affects the flow field.

3. Capillary Filling

3.1. Limit of large times

We first investigate capillary filling dynamics in the limit of large time-scales, with the aim of comparing to the well-known Lucas-Washburn law [16, 17]. In this limit the viscous drag counteracts the driving capillary force and we expect that the filled length l should scale with the square root of time t for sufficiently high viscosity ratio η_w/η_{nw}. We consider a two-dimensional system and assume Poiseuille flow. In this case, the capillary force, $2\gamma\cos\theta^a$, and the viscous drag of the fluid column, $12\eta_w l\frac{dl}{dt}/h$, are balanced to give the Lucas-Washburn law [16, 17]

$$l^2 = \frac{\gamma h\cos\theta^a}{3\eta_w}(t+t_0)\ . \tag{10}$$

Here we use the dynamic contact angle θ^a, since this controls the Laplace pressure across the interface and, as we will show later, is different from the equilibrium contact angle θ^{eq}. Moreover, we expect $\theta^a > \theta^{eq}$, reflecting the fact that

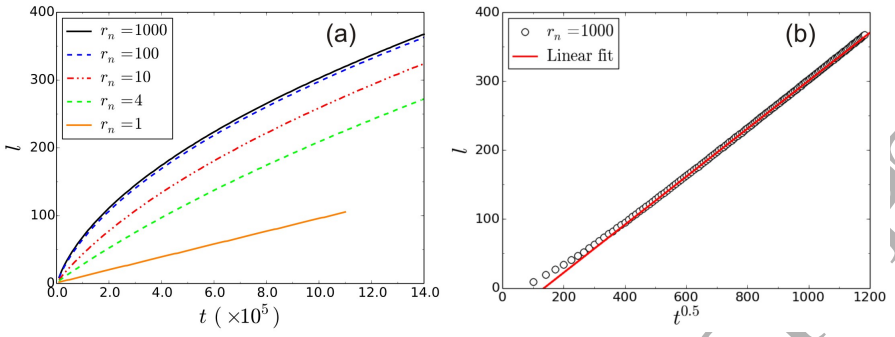

Figure 2: (a) The length of the penetrating fluid column inside the capillary as a function of time for varying viscosity ratio r_n. (b) The length of the penetrating fluid column inside the capillary as a function of the square root of time for viscosity ratio $r_n = 1000$. The solid line is a fit to Washburn's law using the dynamic contact angle at late times from the simulations. Length and time in lattice units.

less energy is available to do useful work than the energy liberated from wetting the channel's surface due to viscous dissipation.

For the case when the viscosity η_{nw} of the resident fluid in the capillary is not negligible, then the viscous drag becomes $12\eta_w l\frac{dl}{dt}/h + 12\eta_{nw}(L-l)\frac{dl}{dt}/h$, reflecting the fact that viscous dissipation in the fluid column ahead of the fluid-fluid interface is increased. In the limit of viscosity ratio 1 ($\eta_w = \eta_{nw}$) this yields the following solution for the filled length

$$l = \frac{\gamma h \cos\theta^a}{6L\eta_w}(t + t_0)\ . \tag{11}$$

As expected l scales linearly with time t, as the viscous dissipation in the channel is independent of the position of the fluid-fluid interface and occurs at approximately the same rate at any given point down the channel.

We consider a channel of length L=640 and width h=50 in lattice units(l.u). All the parameters reported here are in l.u. Later on dimensionless formulation will be denoted with *. Reservoirs of dimensions 460×200 are attached at the inlet and outlet of the channel. Periodic boundary conditions are imposed in the x direction, in order to ensure that the reservoirs are connected and have the same pressure. A schematic representation of the simulation geometry is

shown in Fig. 1. A viscosity ratio $r_\eta = \eta_w/\eta_{nw} = 1000$ is achieved by choosing relaxation times for the two fluids $\tau_w = 2.5$ and $\tau_{nw} = 0.502$, leading to dynamic viscosities $\eta_w = 6.67 \times 10^{-1}$ and $\eta_{nw} = 6.67 \times 10^{-4}$. The other parameters of the simulations are chosen to give $\theta^{eq} = 60°$, $\gamma = 1.17 \times 10^{-2}$ and $\rho_w = \rho_{nw} = 1$. Lower values for the viscosity ratio r_η are achieved by increasing the viscosity of the non-wetting fluid, η_{nw}.

Fig. 2(a) shows the results from simulations for the length of the wetting fluid column as a function of time for varying viscosity ratio r_n. Decreasing r_n by increasing the viscosity of the non-wetting fluid, η_{nw}, results in slowing down the moving interface as the viscous dissipation in the fluid column ahead of the meniscus is increased. For $r_n = 1$ we confirm the linear dependency, eq. 11. Fig. 2(b) shows the results for the length of the column of the filling fluid plotted against the square root of time for $r_n = 1000$. The solid line is a fit to Lucas-Washburn law, verifying that in the limit of high viscosity ratios we recover the theoretically predicted scaling *length* vs. *time*.

Next, we examine the variation of the dynamic contact angle θ^α and its dependency on the velocity of the fluid interface. Cox [60] derived a relation for θ^α, θ^{eq} and the capillary number, $\mathrm{Ca} = \eta_w u/\gamma$, which later on Sheng and Zhou [61] showed that, to lowest order in the capillary number, reduces to

$$\cos(\theta^\alpha) = \cos(\theta^{eq}) - \mathrm{Ca}\ln(KL_s/l_s)\ . \tag{12}$$

K is a constant, L_s is a characteristic lengthscale of the system and l_s is the effective slip length at the contact line.

For high viscosity ratio the interface velocity scales as $1/l$, i.e. the interface slows down as it advances inside the capillary and time progresses, while for $r_n = 1$ the interface moves at a constant velocity. This is evident from Fig. 2(a). Fig. 3(a) shows that for high viscosity ratio ($r_n = 1000$) the dynamic contact angle decreases as time progresses, with initial values being much higher than the equilibrium value of $\theta^{eq} = 60°$. This is consistent with the theoritical prediction [61, 62] as initially the interface is advancing at a higher velocity, thus leading to higher θ^α. For $r_n = 1$ the dynamic angle $\theta^\alpha \sim 61.5°$.

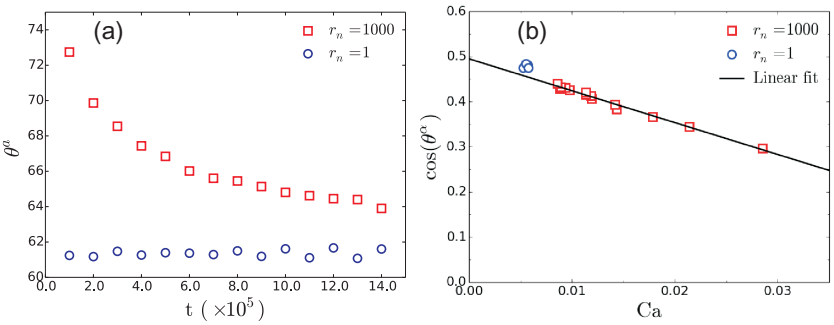

Figure 3: (a) The dynamic contact angle θ^α as a function of time for viscosity ratio $r_n = 1000$ and $r_n = 1$ ($\theta^{eq} = 60°$). (b) The cosine of θ^α plotted against the capillary number Ca. The solid line is a linear fit of $\cos(\theta^\alpha)$ to Ca for $r_n = 1000$.

The linear dependency of $\cos(\theta^\alpha)$ on Ca, predicted by eq. 12, is verified in Fig. 3(b). Fitting the results for $r_n = 1000$ and extrapolating to Ca = 0, reveals $\theta^\alpha_{Ca=0} = 60.3°$ and, hence, the dynamic contact angle tends to the correct value for the equilibrium contact angle of $\theta^{eq} = 60°$.

3.2. Time-stages of capillary filing

In this section we turn our attention to the initial time stages of capillary filling. In terms of dimensional analysis, the following characteristic time-scales can be constructed [18, 31]

$$t_1 \sim \sqrt{\frac{\rho L_s^3}{\gamma}} \text{ and } t_2 \sim \frac{\rho L_s^2}{\eta_w} \,. \tag{13}$$

t_1 is related to initial settling phenomena and the reorientation of the interface at the inlet of the channel to a meniscus when the channel comes into contact with the fluid reservoir. The second time-scale t_2, known as the viscous time-scale, roughly determines the crossover to the viscous regime (Lucas-Washburn regime) for times $t \gg t_2$.

Using these two time-scales, the Ohnesorge number,

$$\text{Oh} = \frac{\eta_w}{\sqrt{\rho \gamma L_s}} \,, \tag{14}$$

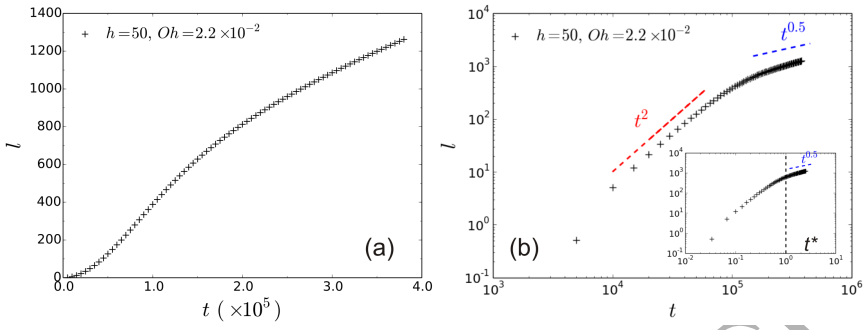

Figure 4: Length of the penetrating fluid column for a simulation with $t_1 = 3.3 \times 10^3$, $t_2 = 1.5 \times 10^5$, Oh $= 2.18 \times 10^{-2}$ and total simulation time $t_{sim} = 4.0 \times 10^5$ (in l.u). All three successive regimes ($l \sim t^2$, $l \sim t$, $l \sim t^{0.5}$) are observed as t_2 is comparable in size with t_{sim}. Dashed lines serve as a guide for the different regimes (short intermediate regime $l \sim t$ not shown on the right subfigure). Inset: *L*ength vs t^* - the transition to the Lucas-Washburn regime occurs at approximately $t^* \sim 1$.

can be obtained as the ratio of the time-scales t_1/t_2. Oh relates the viscous forces to inertial forces and surface tension and is known as a damping measure for capillary dominated oscillations. Depending on the Oh and the relative size of experimental times compared to t_1 and t_2, three successive *length* vs. *time* ($l - t$) regimes can be obtained [28, 31], namely (a) $l \sim t^2$, (b) $l \sim t$ and (c) $l \sim t^{0.5}$. Usually the total experimental time is much larger than the above two time-scales (large Oh) and the Lucas-Washburn regime is obtained. Increasing the two time-scales to the order of the experimental time can make the observation of the first two regimes possible.

Numerically we consider the same geometry as in section 3.1. The viscosity contrast is set to $r_n = 50.5$, by choosing relaxation times for the two fluids $\tau_w = 0.55$ and $\tau_{nw} = 0.501$. This ratio is sufficient to give the Lucas-Washburn regime, $l \sim t^{0.5}$, in the limit of large times ($t \gg t_2$). The other parameters of the simulations are chosen to give $\theta^{eq} = 60°$, $\gamma = 1.17 \times 10^{-2}$ and $\rho_w = \rho_{nw} = 1$.

In order to examine the initial time-stages of capillary filling, we vary the characteristic time-scales by varying the height h of the capillary. Setting $h = 50$ leads to $t_1 = 3.3 \times 10^3$, $t_2 = 1.5 \times 10^5$ and Oh $= 2.18 \times 10^{-2}$. Fig. 4 shows

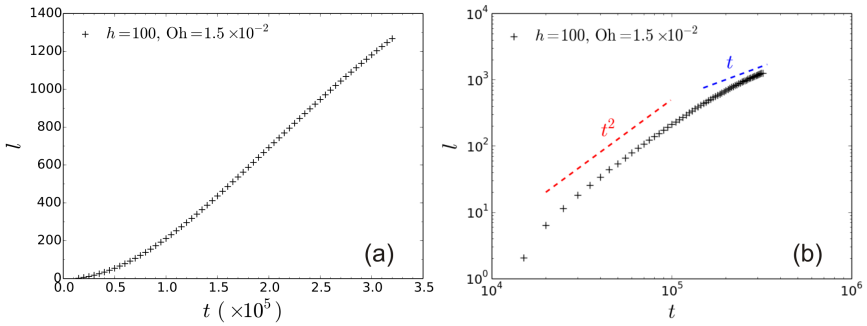

Figure 5: Length of the penetrating fluid column for a simulation with $t_1 = 9.2 \times 10^3$, $t_2 = 6.0 \times 10^5$, Oh $= 1.54 \times 10^{-2}$ and total simulation time $t_{sim} = 3.0 \times 10^5$ (in l.u).

results from a simulation with total simulation time $t_{sim} = 4.0 \times 10^5$. Although $t_{sim} > t_2$, these times are of the same order allowing us to observe all three successive regimes reported experimentally in the literature [28, 31]. When rescaling time with the viscous time-scale, $t^* = t/t_2$, the transition to the Lucas-Washburn regime, $l \sim t^{0.5}$, appears to commence at approximately $t^* \sim 1$, as shown in the inset of Fig. 4. This indicates that t_2 is the appropriate time-scale for evaluating the transition to the Lucas-Washburn regime.

Increasing the height of the channel to $h = 100$ increases the characteristic time-scales, leading to $t_1 = 9.2 \times 10^3$, $t_2 = 6.0 \times 10^5$ and Oh $= 1.54 \times 10^{-2}$. Fig. 5 shows results from a simulation with total simulation time $t_{sim} = 3.0 \times 10^5$. Now, $t_{sim} < t_2$, meaning that there is not enough time now to reach the Lucas-Washburn regime and, hence, we observe first the $l \sim t^2$ regime followed by the $l \sim t$ regime.

Finally, increasing the height of the channel further to $h = 250$ results in $t_1 = 3.7 \times 10^4$, $t_2 = 3.7 \times 10^6$ and Oh $= 9.75 \times 10^{-3}$. Fig. 6 shows results from a simulation with total simulation time $t_{sim} = 1.0 \times 10^5$. In this case the total simulation time is comparable to the first time-scale t_1, enabling us to observe the initial interface fluctuations as can be seen from Fig. 6. Negative values for the interface position correspond to locations within the reservoir, as the mid-position of the interface retracts initially, while the contact line moves inside the

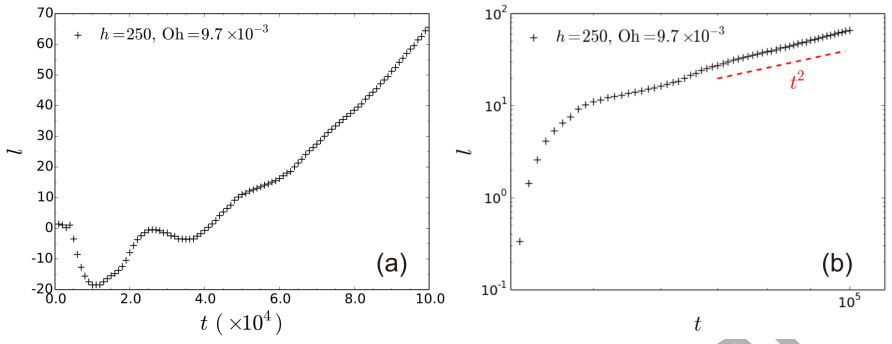

Figure 6: Length of the penetrating fluid column for a simulation with $t_1 = 3.7 \times 10^4$, $t_2 = 3.7 \times 10^6$, Oh $= 9.75 \times 10^{-3}$ and total simulation time $t_{sim} = 1.0 \times 10^5$ (in l.u).

capillary. After the fluctuations-influenced regime, the interface position follows a time squared scaling (see Fig. 6(b)).

3.3. Rescaling - Universal curve

In this section we revisit the limit of large times with the aim of obtaining a universal relation describing the length traveled by the meniscus inside the capillary as a function of time in reduced units. The equation of motion reads

$$0 = F_{cap} - F_{visc} = 2\gamma \cos(\theta^{\alpha}) - \frac{12\eta_w}{h} l \frac{dl}{dt} \, . \tag{15}$$

Rescaling length with the characteristic lengthscale of the system $L_s = h$ and time with the the viscous time-scale leads to

$$\zeta^2 = \frac{\gamma \rho h}{3\eta_w^2} \int \cos(\theta^{\alpha}) dt^* \, , \tag{16}$$

where $\zeta = l/h$ and $t^* = t/t_2$. Identifying the prefactor in front of the time integral as the inverse of Oh leads to

$$l^* = \zeta \times \mathrm{Oh} = \sqrt{\frac{1}{3} \int \cos(\theta^{\alpha}) dt^*} \, . \tag{17}$$

Note here that, contrary to the classical treatment by Lucas [16] and Washburn [17], the dynamic contact angle depends on time, as shown in section 3.1.

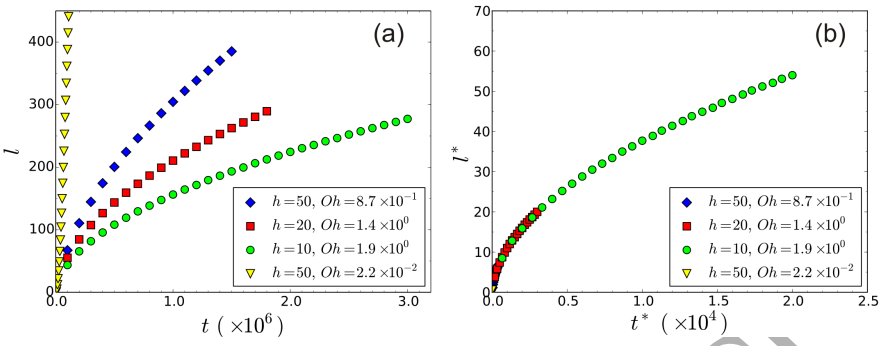

Figure 7: (a) Length of the penetrating fluid column for simulations with $\theta^{eq} = 60°$ and channels with different heights. (b) *L*ength vs *T*ime in reduced units. Results collapse on a single curve.

In order to examine the validity of eq. 17 we carry out simulations with viscosity ratio $r_n = 1000$ ($\tau_w = 2.5$, $\tau_{nw} = 0.502$) and equilibrium contact angles $\theta^{eq} = 20°, 60°$. Fig. 7 shows the results for $\theta^{eq} = 60°$ and varying channel heights h. The wetting fluid penetrates at a faster rate with increasing channel height, if all other parameters are kept fixed, consistent with the predictions of eq. 10. Triangles denote results from a simulation with a wetting fluid with smaller viscosity. As expected from eq. 10 the interface advances faster in this case. Results for $\theta^{eq} = 20°$ are qualitatively the same.

When results are plotted in reduced units, see Fig. 7(b), then a single curve describes the imbibition length. This implies that the integral $\int \cos(\theta^{\alpha}) dt^*$ in eq. 17 is roughly identical for all simulations irrespective of the different channel heights. In other words the dynamic contact angle scales in the same way with the rescaled time t^* and the only lengthscale dependency is included in the Ohnesorge number. This is verified from Fig. 8(b). Moreover, the dynamic contact angle approaches the equilibrium value much more rapidly for smaller channel heights as shown in Fig. 8(a). This can be explained considering the dependency of θ^{α} on the interface velocity. Increasing channel height increases interface velocity, thus leading to higher Ca and larger θ^{α}, i.e. smaller $\cos(\theta^{\alpha})$.

Finally, results for the imbibition length for varying equilibrium contact

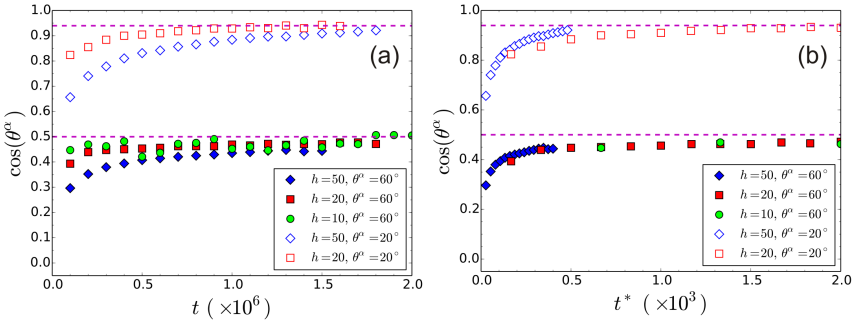

Figure 8: (a) The cosine of the dynamic contact angle as a function of time for simulations with $\theta^{eq} = 20°$, 60° and channels with different heights. (b) The same plot in reduced units. The dashed lines are the corresponding values for the cosines of the equilibrium contact angles.

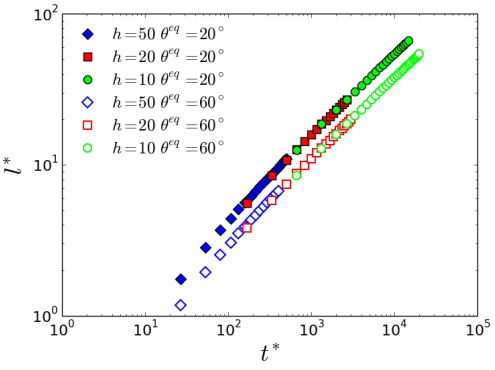

Figure 9: *L*ength vs *T*ime in reduced units for simulations with $\theta^{eq} = 20°$ and 60°.

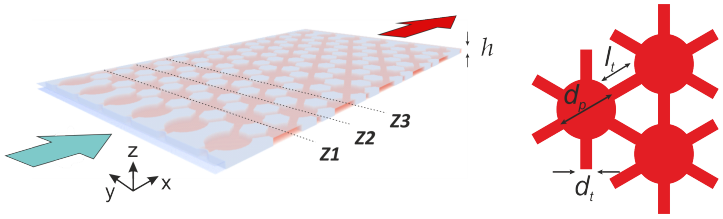

Figure 10: The geometry used in the LB simulations. Velocity boundary conditions are applied in the inlet and outlet of the simulation domain to drive the flow, while periodic boundary conditions are imposed in the y direction. In the z direction walls are located at z=0 and z=h.

angles ($\theta^{eq} = 20°, 60°$) are shown in Fig. 9. The interface advances faster for $\theta^{eq} = 20°$ consistent with the higher driving force and results are described by two distinct paths. The collapse of results from simulations with fixed θ^{eq}, when analysed in terms of rescaled lengths and times, provides a useful tool for predicting the imbibition length in experiments when a single set of results is known.

4. Haines jump events

We next proceed to investigate the dynamics of Haines jumps events [9], which can occur during drainage. Whether drainage can be considered as a cascade of events where the pore space is invaded by a non-wetting fluid pore-by-pore while neglecting the dynamics of the process in order to simplify things is becoming increasingly questioned. Pore-network modeling, which takes advantage of a decomposition of the pore space in an ensemble of geometric shapes that drain in a sequential manner, based on the capillary entry pressures, neglects dynamical effects at the pore-scale. However, dynamical effects due to pore-scale instabilities can alter the displacement pathways [10] or lead to fluid redistribution at a time-scale comparable to the time-scale of general advancement of fluid front propagation [6], and hence the quasistatic approach used in pore-network modeling may not be able to predict correctly the residual saturation after drainage and imbibition. Considering that capillary or viscous forces

may not be acting in a purely local way, as demonstrated recently [5, 6], this illustrates the importance of considering the full dynamics at the pore-scale for modeling displacement processes.

During drainage the pressure generally increases steadily. However, as the non-wetting phase travels through a narrow throat to a wider pore-body, because it exceeds the capillary entry pressure, the pressure drops instantaneously and the pore-space fills quickly. Recent developments in synchrotron-based X-ray computed microtomography improved the temporal resolution in the range of seconds, enabling the imaging of pore-scale displacement events while maintaining the flow, the pressure gradients and the viscocapillary balance during imaging [5]. This offers the possibility to directly visualise rapid events, such as the Haines jumps, and other pore-scale displacement events in porous rock in real time. These rapid events are very important to the upscaling of multiphase flow, since they account for a significant fraction of the energy dissipation within the system [63, 5]. Moreover, although often questioned, as an irreversible displacement process, they may also contribute to macroscopic properties of the rock such as the relative permeability [64].

4.1. Haines jumps in simplified geometries

Here, as a first step, we investigate whether the LB method can capture the dynamics involved in this dynamical process. Fig. 10 shows the geometry used in the three dimensional simulations. In order to drive the drainage process, the injected non-wetting phase (blue) enters the simulation domain at a given flow rate $Q = \int\int_A \mathbf{u}\cdot d\mathbf{A}$ at the inlet, while imposing the same flow rate at the outlet allows the wetting phase (red) to exit the system. The geometry is effectively a Hele-Shaw cell with walls located at z=0 and z=h=10 l.u, platelets of diameter $d_p = 60$ l.u. as the wider pore-bodies and 6 throats of width $d_t = 12$ l.u. and length $l_t = 22$ l.u. connecting the pore bodies. Small reservoirs of length 16 l.u. are added at the inlet and the outlet. Simulations were performed using fluids of the same viscosity, while the equilibrium contact angle was set to $\theta^{eq} = 30°$ and 60°. Fig. 11(a) shows consecutive snapshots from simulations during drainage,

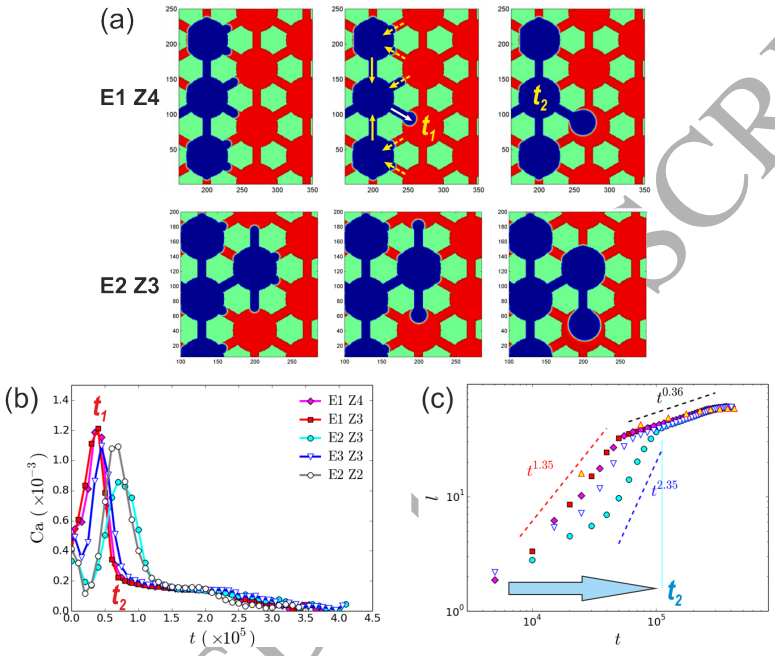

Figure 11: (a) Illustration of Haines jumps events [9] during drainage. Pore drainage event is labeled with white arrow, meniscus recession is labeled with dotted yellow arrows and the flow direction is labeled with the yellow arrows. En Zc stands for the n_{th} event in zone c, where zone labels the distance from the inlet (see Fig. 10). (b) The capillary number Ca versus time during several pore drainage events from a simulation with injection flow rate $Q_h \sim 10^{-1}$ (l.u.). (c) The distance traveled by the interface versus time during jump events in (b). Results (E1 Z3) from a simulation with a lower injection flow rate $Q_l \sim 10^{-2}$ (l.u.) are shown with yellow triangles. The two fluids have the same viscosity $\eta_w = \eta_{nw} = 1.67 \times 10^{-2}$, surface tension $\gamma = 1.17 \times 10^{-2}$ (l.u.) and $\theta^{eq} = 30°$.

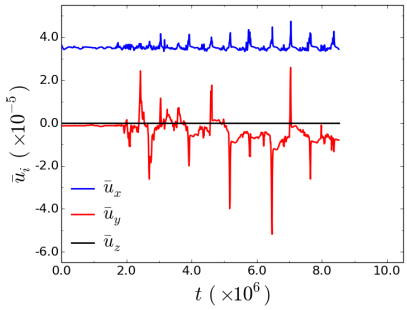

Figure 12: The average components of the velocity $\bar{u}_i$ during drainage. The peaks denote the occurrence of Haines jumps. The flow is in the x-direction. Non-zero values for $\bar{u}_y$ denote jumps perpendicular to the direction of the flow, which if averaged over longer times it is expected to be zero.

where Haines jumps events are observed. During the drainage of a pore-body, imbibition occurs in the neighboring throats and the fluid interface retracts as shown by the dotted yellow arrows. These imbibition events provide a fraction of the fluid necessary for draining the pore-body and lead to rearrangement of the fluids in the surrounding area of a pore drainage event. These observations are in agreement with recent experiments by Armstrong and Berg [6] and demonstrate that pore drainage dynamics are cooperative and nonlocal, since they extend beyond the draining pore-body.

Examining the flow field during a jump event reveals that the fluid-fluid interface velocity is larger than the mean fluid velocity. This is demonstrated in Fig. 11(b), where we analyse the magnitude of the velocity field during several events from the same simulation, and in Fig. 12 where we plot the average components of the velocity $\bar{u}_i$ $(i = x, y, z)$ during drainage. When the non-wetting fluid reaches the wider pore-body and the pressure exceeds the pore entry pressure, the interface "jumps" into the pore body accelerating until it reaches a maximum velocity $(t = t_1)$ and then decelerates. This initial acceleration is due to the viscous resistance of the resident wetting fluid in the pore body and inertial forces being too small to resist the rapid fluid motion driven by capillary

forces. Differences in the curvature of the meniscus in the pore body and the menisci in the surrounding throats generate high transient pressure gradients and therefore capillary forces act in a nonlocal way, since a capillary pressure difference can exist over multiple pores [6].

The events shown in Fig. 11(a) have different fluid distributions prior to the Haines jump event. The first column corresponds to the beginning of the events ($t = t_0$), the second one to the time of maximum interfacial velocity ($t = t_1$), while the third one denotes the time when all the non-wetting fluid from the surrounding pore throats was provided for draining the pore body ($t = t_2$) and marks the end of fluid rearrangement during a Haines jump event. It is evident from Fig. 11(b),(c) that the fluid distributions prior to the jump event affects both the scaling of length with time, as well as the time-scale over which higher interfacial velocities are obtained, $t_0 \leq t \leq t_2$. Results from events with similar fluid distributions prior the event (see E1 Z3, E1 Z4) completely overlap. Nevertheless, after fluid rearrangement has completed ($t = t_2$) all results collapse.

The bulk pressure field p_b during a Haines jump event is shown in Fig. 13 (middle panel). This reveals the pressure drop during the onset of the event, as well as the differences in capillary forces between the meniscus in the draining pore-body and the neighboring throats, throughout the duration of the drainage event. This is shown more clearly in the last column where we plot the pressure field along the lines shown in the middle panel. Examining further the pressure differences ΔP developed due to differences in the curvature of the advancing meniscus and the receding menisci, we clearly see in Fig. 14, that the duration of higher interfacial velocities coincides with the duration of these transient pressure gradients and the fluid redistribution in the neighboring area.

Gauglitz and Radke [65] demonstrated the importance of the Ohnesorge number during Haines jump events for compressible bubbles. The Ohnesorge number gives the ratio of viscous forces over inertia and surface tension, i.e. Oh = viscous forces / (inertia $\times$ surface tension)$^{0.5}$ $= \eta_w/\sqrt{\rho\gamma d_t}$. Considering the relevant forces during a jump event, we can identify that after $t = t_1$ the driving

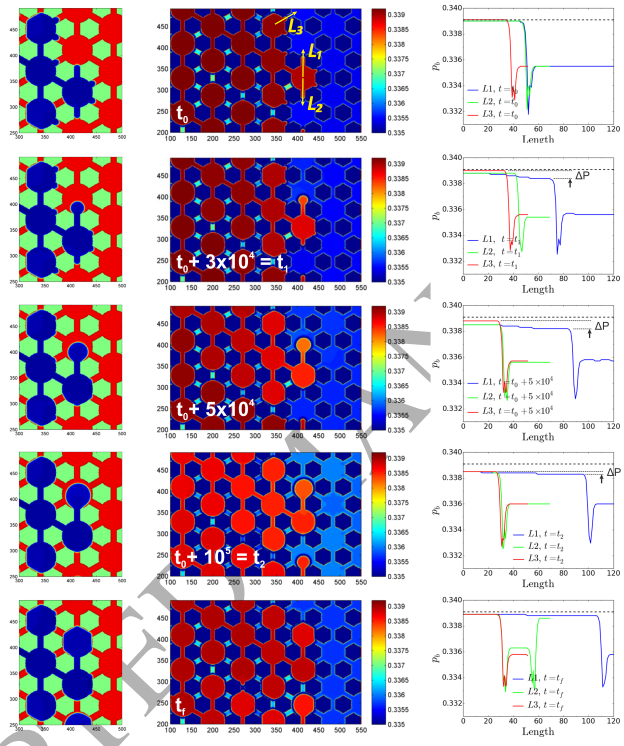

Figure 13: Concentration (left panel) and pressure field (center panel) during a Haines jump event (E2 Z5). Right panel: The pressure field p_b along the lines $L1$ (draining pore), $L2$, $L3$ (surrounding throats), shown in the middle panel. Times t_0, t_1, t_2, t_f denote the onset of the event, the time of maximum interfacial velocity, the time when fluid rearrangement was completed and the draining time respectively.

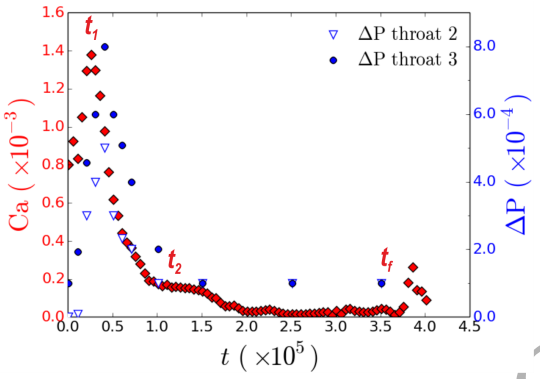

Figure 14: The capillary number Ca as a function of time and the pressure difference between the meniscus in the draining pore body and the menisci in the two neighbouring throats (along lines $L2$, L_3) for the event shown in Fig. 13. For comparison reasons, the maximum pressure gradient generated is $\sim 7 \times 10^{-6}$ (l.u.), while the inlet-outlet maximum pressure gradient is $\sim 4.5 \times 10^{-6}$(l.u.). The time-scale of high interfacial velocity (t_2) coincides with the time-scale of high local pressure gradients.

forces are capillary and inertial forces, while viscous forces are the resisting ones; hence, for times $t > t_1$, Oh should be controlling the dynamics of these events. Moreover, since the total draining time is much larger than t_1, then effectively Oh controls the time-scale of draining the pore-bodies. This explains the experimental observation [6] that, for a given system of fluids, the pores drain on the same time-scale regardless of the externally imposed capillary number, since there is no flow rate dependency in Oh. This is verified in Fig. 11(c) where we show results from simulations with two different injection flow rates $Q_h \sim 10^{-1}$, $Q_l \sim 10^{-2}$.

We can also understand the above by considering the following. The drainage process can be divided into two flow regimes: a) when the interface moves in the pore throats and b) when the interface moves from a throat (narrow restriction) to a wider pore body. During the first flow regime, which can be reversible and controlled by the injection flow rate, energy is stored in the menisci and the fluid columns of the non-wetting phase in the pore throats due to the work done by the external forces. This energy is then released during the Haines jump

event (second flow regime), converted into kinetic energy and surface energy and dissipated. Therefore, for a given geometry and fluids, approximately the same amount of energy will be stored in the menisci and then released, irrespective of the externally imposed flow rate, leading to the same draining times.

As demonstrated earlier in section 3, the Ohnesorge number also affects the early dynamics of capillary filling and the scaling of the penetrating length of the wetting fluid as a function of time. This will in turn affect here the rate at which non-wetting fluid is provided for the drainage event from the imbibition events occurring in surrounding throats and consequently the dynamics of the Haines jumps event. Therefore, an important remark regarding the modeling of these rapid pore-scale events, is that if a suitable choice of parameters is not made to match the relevant dimensionless parameters, such as Oh, or the time-scales for Haines jumps and imbibition dynamics, then the dynamics of imbibition in the neighboring throats that control the initial stages of the jump and the fluid rearrangement will not be correctly resolved.

4.1.1. The role of viscous and capillary forces

Next we investigate Haines jumps events in simplified two-dimensional geometries and examine the impact of viscous and capillary forces, quantified through the Ohnesorge number, on the onset of the phenomenon. In each simulation the viscosity ratio is set to $r_n = \eta_w/\eta_{nw} = 1$, while we vary the Oh by varying mainly the viscosity of the fluids and the surface tension. For all simulations $\theta^{eq} = 60°$. As a characteristic lengthscale we use the throat diameter d_t, since this controls the capillary entry pressure. The role of the viscosity contrast will be examined in future work.

Fig. 15 shows the results from simulations for varying Oh. Run(a) corresponds to a simulation with $\eta_w = 1.67 \times 10^{-3}$ and $\gamma = 1.17 \times 10^{-2}$ leading to $\mathrm{Oh} = 4.45 \times 10^{-3}$ ($\mathrm{Ca} \sim 5 \times 10^{-4}$, $\mathrm{Re} \sim 2.2 \times 10^{1}$). A Haines jump event is clearly observed as the pore-body drains. Note that initially the two throats are completely filled with the non-wetting fluid and then the meniscus retracts in the upper throat. Increasing the viscosity to $\eta_w = 1.67 \times 10^{-1}$ in run(b) and

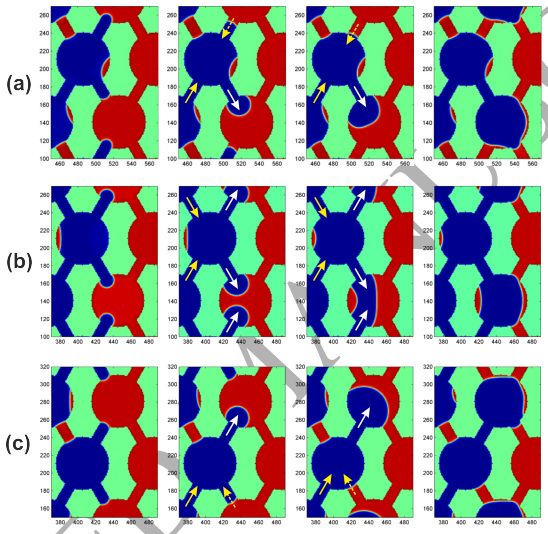

Figure 15: Simulations with varying Ohnesorge number. Pore drainage events are labeled with white arrows, meniscus recession is labeled with dotted yellow arrows and the flow direction is labeled with the yellow arrows. Haines jump events are observed in (a) and (c). (a) $\mathrm{Oh} = 4.45 \times 10^{-3}$ ($\mathrm{Ca} \sim 5 \times 10^{-4}$, $\mathrm{Re} \sim 2.2 \times 10^{1}$). (b) $\mathrm{Oh} = 4.45 \times 10^{-1}$ ($\mathrm{Ca} \sim 2 \times 10^{-3}$, $\mathrm{Re} \sim 9 \times 10^{-3}$). (c) $\mathrm{Oh} = 3.15 \times 10^{-1}$ ($\mathrm{Ca} \sim 2 \times 10^{-3}$, $\mathrm{Re} \sim 2 \times 10^{-2}$).

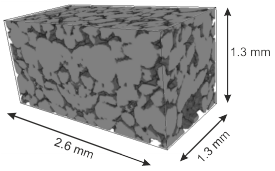

Figure 16: The Bentheimer sandstone sample used in the LB simulations. This is filled with the wetting phase, while reservoirs with the non-wetting phase are attached to the inlet and outlet of the sample.

keeping all other parameters fixed leads to Oh $= 4.45 \times 10^{-1}$ (Ca $\sim 2 \times 10^{-3}$, Re $\sim 9 \times 10^{-3}$). This increases the viscous resistance of the wetting fluid, hence suppressing any rapid movement of the interface and eventually the onset of a Haines jump event. Finally in run(c) we keep all parameters as in run(b) and increase surface tension to $\gamma = 2.34 \times 10^{-2}$ (Oh $= 3.15 \times 10^{-1}$, Ca $\sim 2 \times 10^{-3}$, Re $\sim 2 \times 10^{-2}$). This in turn increases the driving capillary forces and leads to recurrence of the phenomenon. An alternative way of considering the Haines jumps events is that during drainage elastic potential energy is stored in the fluid-fluid interface up to a given threshold, which is then released resulting in irreversible fluid rearrangement, and dissipated in the system. Here, increasing the viscosity in (b) results in increased viscous dissipation rate, which suppresses rapid interfacial motion. Finally, increasing the surface tension in run(c) increases the elastic energy initially contained in the liquid-liquid menisci which is then converted into kinetic energy and finally dissipated.

4.2. Haines jumps in rock samples

We further proceed to run direct simulations of two-phase flow on micro-CT images of a Bentheimer rock sample with a spatial resolution of 5.1 μm. A sequence of snapshots from simulations during drainage is shown in Fig. 17. Both fluids have the same viscosity, Ca $\sim 1 \times 10^{-4}$ and $\theta^{eq} = 35°$. We consider a situation which is capillary-inertial controlled by choosing Oh $\sim 10^{-3}$. Berg et *al.* [5] who investigated Haines jumps experimentally in Berea sandstone using water (wetting fluid) and n-decane (non-wetting), quantify the importance of

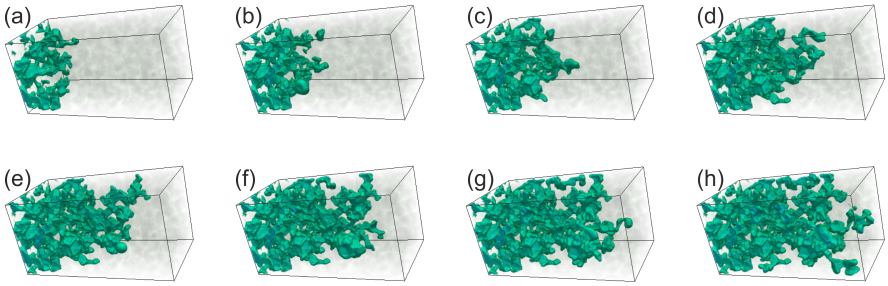

Figure 17: Sequence of snapshots from LB simulations during drainage of Bentheimer sandstone at time intervals of $dt = 5 \times 10^4$ l.u. ($\mathrm{Ca} \sim 1 \times 10^{-4}$, $\mathrm{Oh} \sim 10^{-3}$ and $\theta^{eq} = 35°$).

the relevant forces using the ratio of Re/Ca, which is related to Oh as $\mathrm{Re/Ca} = \mathrm{Oh}^{-2}$, and report experimental values of $\mathrm{Re/Ca} \sim 2 \times 10^3$ ($\mathrm{Oh} = 2.2 \times 10^{-2}$).

In order to identify whether fluid rearrangement takes place during draining a pore, indicative of a Haines jump event, we subtract consecutive images before (Fig. 18(a)) and after (Fig. 18(b)) several pores drain. This is shown in Fig. 18(c), where regions in blue denote the draining pores and regions in red reveal the locations where imbibition took place. A more detailed analysis on Haines jump events at the pore-scale and its consequences for larger scales, which is today often questioned, will be the subject of future investigation.

With regards to CO_2 geological sequestration, numerical modeling must match the relevant dimensionless parameters and the relative magnitude of timescales in order to ensure that any predictions will be valid and accurate. Here we give a brief overview of the details involved [66]. The injection depth, which for saline aquifers is in the range of 800 m - 3 000 m, affects the temperature and the pressure. In these depths the CO_2 exists in a supercritical state. The density of water may vary from $\rho_{wa} = 945$ to 1230 kgm^{-3}, while the corresponding density of CO_2 varies from $\rho_c = 266$ to 733 kgm^{-3}. Correspondingly the dynamic viscosities for water and CO_2 may vary in the range $\eta_{wa} = 0.195 - 1.58 mPa \cdot s$ and $\eta_c = 0.023 - 0.0611 mPa \cdot s$ respectively. Thus, the ratio for the densities and viscosities vary in the range $\rho_{wa}/\rho_c = 0.22 - 0.75$ and $\eta_{wa}/\eta_c = 0.026 - 0.22$ [67]. The interfacial tension for water - CO_2 $\gamma \sim 30$ mNm^{-1}. Using a char-

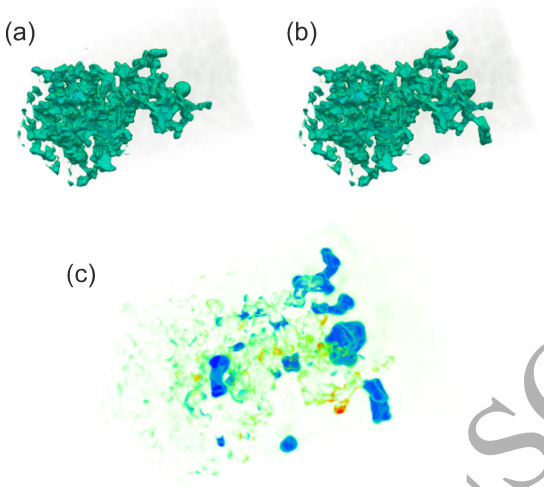

Figure 18: Snapshots from LB simulations (a) before and (b) after drainage events of Bentheimer sandstone. (c) Subtracting the two images reveals the draining pores (blue) as well as the locations of imbibition and the rearrangement of the wetting phase (red) in the areas upstream.

acteristic lengthscale of d_t ~10-100μm and average velocity $u \sim 1\mu m/s$ yields Ca $= \eta_{wa}u/\gamma \sim 10^{-8}$, Oh $= \eta_{wa}/\sqrt{\rho_{wa}\gamma d_t} \sim 3 \times 10^{-3}$ to 9×10^{-2} and viscous time-scale $t_v = \rho_{wa}d_t^2/\eta_{wa} \sim 10^{-5} - 10^{-1}s$.

5. Conclusions

The occurrence of Haines jump events is a characteristic feature of multiphase flow in porous media, primarily associated with drainage dynamics. These events are accompanied by an abrupt increase in the fluid velocity, as the interface jumps from a narrow restriction into a wider pore body. This leads to fluid redistribution in the surrounding area of a draining pore, as a significant fraction of the non-wetting phase, required to drain the pore-body, is supplied by imbibition occurring in the neighboring pore throats.

In this work, we investigated the dynamics of Haines jump events using free energy Lattice Boltzmann simulations. Since these interfacial jumps are associated with both drainage and imbibition dynamics, we first turned our

attention to capillary filling dynamics and the dynamics of a fluid penetrating a hydrophilic channel. Our investigation covered: a) the limit of large times for both high and low viscosity ratios r_n, b) the limit of small times. Results demonstrated that the numerical scheme can capture the correct dynamics for capillary filling as the agreement with theory is excellent. Correct scaling of *length* vs *time* is observed in the limit of large times; $l \sim t^{0.5}$ for high viscosity ratios, $r_n = \eta_w/\eta_{nw}$, and $l \sim t$ in the limiting case of $r_n = 1$. In the limit of small times, and for sufficiently high viscosity ratio, two consecutive regimes can be obtained preceding the viscous or Lucas-Washburn regime ($l \sim t^{0.5}$), namely a. inertial regime ($l \sim t^2$) and b. visco-inertial regime ($l \sim t$), depending on the relative size of the total filling time and the viscous time-scale.

Turning our attention to the Haines jumps problem, we verified that these rapid events are associated with both drainage and imbibition dynamics. High pressure gradients, generated due to differences in the curvatures of the menisci, drive this interfacial instability. As the fluid velocity during a Haines jump event can be much larger than the average velocity, correctly capturing the displacement process requires solving the full Navier Stokes equations.

Examining the duration of higher interfacial velocities during a Haines jump event revealed that this coincides with the end of fluid rearrangement in the surrounding pore throats. Hence, this is determined by the amount of non-wetting phase in the neighbouring pore throats and the time-scale over which high transient pressure gradients can be sustained.

Finally, we identified the Ohnesorge number as an important controlling parameter for the identification of the type of pore filling dynamics that will occur. Fluid flow that is capillary-inertial controlled, i.e. characterised by small Ohnesorge number, can lead to the occurrence of Haines jump events, while fluid flow at larger Ohnesorge numbers lead to fluid flow that is controlled by viscous forces and shows a distinctively different displacement process. Therefore, careful examination of the relevant parameters, such as the Ohnesorge number, is necessary in order to ensure that the dynamics of both capillary filling and Haines jumps will be correctly captured. In this paper, we carefully analysed

single pore filling events. Our examinations were extended to rock samples with multiple pores; a more detailed analysis will be reported in a forthcoming paper. We have reason to believe that an accurate description of single pore filling dynamics may affect the displacement processes at the continuum / Darcy scale.

Acknowledgements

The authors thank the sponsors of this research: Qatar Petroleum, Shell and the Qatar Science and Technology Park under the Qatar Carbonates and Carbon Storage Research Centre (QCCSRC).

References

[1] M. Muskat, M. Meres, The flow of heterogeneous fluids through porous media, Journal of Applied Physics 7 (9) (1936) 346–363. doi:10.1063/1.1745403.

[2] R. Wyckoff, H. Botset, The Flow of Gas-Liquid Mixtures Through Unconsolidated Sands, Journal of Applied Physics 7 (9) (1936) 325–345. doi:10.1063/1.1745402.

[3] M. Leverett, Flow of oil-water mixtures through unconsolidated sands, Transactions of the AIME 132 (01) (1939) 149–171. doi:10.2118/939149-G.

[4] G. Barenblatt, T. Patzek, D. Silin, The mathematical model of nonequilibrium effects in water-oil displacement, SPE Journal 8 (04) (2003) 409–416. doi:10.2118/87329-PA.

[5] S. Berg, H. Ott, S. A. Klapp, A. Schwing, R. Neiteler, N. Brussee, A. Makurat, L. Leu, F. Enzmann, J.-O. Schwarz, M. Kersten, S. Irvine, M. Stampanoni, Real-time 3D imaging of Haines jumps in porous media flow, Proceedings of the National Academy of Sciences 110 (10) (2013) 3755–3759. doi:10.1073/pnas.1221373110.

[6] R. T. Armstrong, S. Berg, Interfacial velocities and capillary pressure gradients during Haines jumps, Physical Review E 88 (4) (2013) 043010. doi:10.1103/PhysRevE.88.043010.

[7] R. T. Armstrong, N. Evseev, D. Koroteev, S. Berg, Modeling the velocity field during Haines jumps in porous media, Advances in Water Resources 77 (0) (2015) 57 – 68. doi:10.1016/j.advwatres.2015.01.008.

[8] H. Yamabe, T. Tsuji, Y. Liang, T. Matsuoka, Lattice Boltzmann Simulations of Supercritical CO2 - Water Drainage Displacement in Porous Media: CO2 Saturation and Displacement Mechanism, Environmental Science & Technology 49 (1) (2015) 537–543, pMID: 25427299. doi:10.1021/es504510y.

[9] W. B. Haines, Studies in the physical properties of soil. V. The hysteresis effect in capillary properties, and the modes of moisture distribution associated therewith, The Journal of Agricultural Science 20 (01) (1930) 97–116. doi:10.1017/S002185960008864X.

[10] A. Ferrari, I. Lunati, Inertial effects during irreversible meniscus reconfiguration in angular pores, Advances in Water Resources 74 (2014) 1 – 13. doi:10.1016/j.advwatres.2014.07.009.

[11] M. R. Swift, W. R. Osborn, J. M. Yeomans, Lattice Boltzmann simulation of nonideal fluids, Phys. Rev. Lett. 75 (5) (1995) 830–833. doi:10.1103/PhysRevLett.75.830.

[12] M. R. Swift, E. Orlandini, W. R. Osborn, J. M. Yeomans, Lattice Boltzmann simulations of liquid-gas and binary fluid systems, Phys. Rev. E 54 (5) (1996) 5041–5052. doi:10.1103/PhysRevE.54.5041.

[13] J. Han, H. G. Craighead, Separation of long DNA molecules in a microfabricated entropic trap array, Science 288 (5468) (2000) 1026–1029. doi:10.1126/science.288.5468.1026.

[14] D. Janasek, J. Franzke, A. Manz, Scaling and the design of miniaturized chemical-analysis systems, Nature 442 (7101) (2006) 374–380. doi:10.1038/nature05059.

[15] A. Demello, Control and detection of chemical reactions in microfluidic systems., Nature 442 (7101) (2006) 394–402. doi:10.1038/nature05062.

[16] R. Lucas, Rate of capillary ascension of liquids, Kolloid Z 23 (15) (1918) 15–22.

[17] E. W. Washburn, The Dynamics of Capillary Flow, Phys. Rev. 17 (1921) 273–283. doi:10.1103/PhysRev.17.273.

[18] D. Quéré, Inertial capillarity, EPL (Europhysics Letters) 39 (5) (1997) 533. doi:10.1209/epl/i1997-00389-2.

[19] F. Diotallevi, L. Biferale, S. Chibbaro, G. Pontrelli, F. Toschi, S. Succi, Lattice Boltzmann simulations of capillary filling: finite vapour density effects, The European Physical Journal-Special Topics 171 (1) (2009) 237–243. doi:10.1140/epjst/e2009-01034-6.

[20] P. Raiskinmki, A. Shakib-Manesh, A. Jsberg, A. Koponen, J. Merikoski, J. Timonen, Lattice-Boltzmann Simulation of Capillary Rise Dynamics, Journal of Statistical Physics 107 (1-2) (2002) 143–158. doi:10.1023/A:1014506503793.

[21] S. Levine, J. Lowndes, E. J. Watson, G. Neale, A theory of capillary rise of a liquid in a vertical cylindrical tube and in a parallel-plate channel: Washburn equation modified to account for the meniscus with slippage at the contact line, Journal of Colloid and Interface Science 73 (1) (1980) 136 – 151. doi:10.1016/0021-9797(80)90131-9.

[22] D. I. Dimitrov, A. Milchev, K. Binder, Capillary Rise in Nanopores: Molecular Dynamics Evidence for the Lucas-Washburn Equation, Phys. Rev. Lett. 99 (2007) 054501. doi:10.1103/PhysRevLett.99.054501.

[23] C. M. Pooley, H. Kusumaatmaja, J. M. Yeomans, Contact line dynamics in binary lattice Boltzmann simulations, Phys. Rev. E 78 (2008) 056709. doi:10.1103/PhysRevE.78.056709.

[24] M. Stukan, P. Ligneul, J. Crawshaw, E. Boek, Spontaneous imbibition in nanopores of different roughness and wettability, Langmuir 26 (16) (2010) 13342–13352. doi:10.1021/la101995t.

[25] H. Kusumaatmaja, C. M. Pooley, S. Girardo, D. Pisignano, J. M. Yeomans, Capillary filling in patterned channels, Phys. Rev. E 77 (2008) 067301. doi:10.1103/PhysRevE.77.067301.

[26] B. M. Mognetti, J. M. Yeomans, Capillary filling in microchannels patterned by posts, Phys. Rev. E 80 (2009) 056309. doi:10.1103/PhysRevE.80.056309.

[27] R. Siegel, Transient capillary rise in reduced and zero-gravity fields, Journal of Applied Mechanics 28 (2) (1961) 165–170. doi:10.1115/1.3641647.

[28] M. Dreyer, A. Delgado, H.-J. Path, Capillary rise of liquid between parallel plates under microgravity, Journal of Colloid and interface science 163 (1) (1994) 158–168. doi:10.1006/jcis.1994.1092.

[29] N. Ichikawa, Y. Satoda, Interface dynamics of capillary flow in a tube under negligible gravity condition, Journal of colloid and interface science 162 (2) (1994) 350–355. doi:10.1006/jcis.1994.1049.

[30] B. Zhmud, F. Tiberg, K. Hallstensson, Dynamics of capillary rise, Journal of Colloid and Interface Science 228 (2) (2000) 263–269. doi:10.1006/jcis.2000.6951.

[31] M. Stange, M. E. Dreyer, H. Rath, Capillary driven flow in circular cylindrical tubes, Physics of Fluids (1994-present) 15 (9) (2003) 2587–2601. doi:10.1063/1.1596913.

[32] M. J. Blunt, M. D. Jackson, M. Piri, P. H. Valvatne, Detailed physics, predictive capabilities and macroscopic consequences for pore-network models of multiphase flow, Advances in Water Resources 25 (812) (2002) 1069 – 1089. doi:10.1016/S0309-1708(02)00049-0.

[33] M. J. Blunt, B. Bijeljic, H. Dong, O. Gharbi, S. Iglauer, P. Mostaghimi, A. Paluszny, C. Pentland, Pore-scale imaging and modelling, Advances in Water Resources 51 (2013) 197 – 216, 35th Year Anniversary Issue. doi:10.1016/j.advwatres.2012.03.003.

[34] C. Hirt, B. Nichols, Volume of fluid (VOF) method for the dynamics of free boundaries, Journal of Computational Physics 39 (1) (1981) 201 – 225. doi:10.1016/0021-9991(81)90145-5.

[35] W. J. Rider, D. B. Kothe, Reconstructing Volume Tracking, Journal of Computational Physics 141 (2) (1998) 112 – 152. doi:10.1006/jcph.1998.5906.

[36] A. Ferrari, I. Lunati, Direct numerical simulations of interface dynamics to link capillary pressure and total surface energy, Advances in Water Resources 57 (2013) 19 – 31. doi:10.1016/j.advwatres.2013.03.005.

[37] S. Osher, J. A. Sethian, Fronts propagating with curvature-dependent speed: Algorithms based on Hamilton-Jacobi formulations, Journal of Computational Physics 79 (1) (1988) 12 – 49. doi:10.1016/0021-9991(88)90002-2.

[38] M. Sussman, P. Smereka, S. Osher, A Level Set Approach for Computing Solutions to Incompressible Two-Phase Flow, Journal of Computational Physics 114 (1) (1994) 146 – 159. doi:10.1006/jcph.1994.1155.

[39] G. Doolen, Lattice gas methods for partial differential equations: a volume of lattice gas reprints and articles, including selected papers from the Workshop on Large Nonlinear Systems, held August, 1987 in Los Alamos, New Mexico, Vol. 4, Addison-Wesley Longman, 1990.

[40] R. Benzi, S. Succi, M. Vergassola, The lattice Boltzmann equation: theory and applications, Physics Reports 222 (3) (1992) 145–197. doi:10.1016/0370-1573(92)90090-M.

[41] S. Chen, Z. Wang, X. Shan, G. D. Doolen, Lattice Boltzmann computational fluid dynamics in three dimensions, Journal of Statistical Physics 68 (3-4) (1992) 379–400. doi:10.1007/BF01341754.

[42] S. Succi, The Lattice-Boltzmann Equation, Oxford university press, Oxford, 2001.

[43] R. Benzi, S. Succi, M. Vergassola, The lattice Boltzmann equation: theory and applications, Physics Reports 222 (3) (1992) 145 – 197. doi:DOI: 10.1016/0370-1573(92)90090-M.

[44] C. M. Pooley, K. Furtado, Eliminating spurious velocities in the free-energy lattice Boltzmann method, Phys. Rev. E 77 (2008) 046702. doi:10.1103/PhysRevE.77.046702.
URL http://link.aps.org/doi/10.1103/PhysRevE.77.046702

[45] J. Yeomans, Mesoscale simulations: Lattice Boltzmann and particle algorithms, Physica A: Statistical and Theoretical Physics 369 (1) (2006) 159 – 184. doi:10.1016/j.physa.2006.04.011.

[46] S. A. Setu, I. Zacharoudiou, G. J. Davies, D. Bartolo, S. Moulinet, A. A. Louis, J. M. Yeomans, D. G. A. L. Aarts, Viscous fingering at ultralow interfacial tension, Soft Matter 9 (2013) 10599–10605. doi:10.1039/C3SM51571K.

[47] S. A. Setu, R. P. Dullens, A. Hernández-Machado, I. Pagonabarraga, D. G. Aarts, R. Ledesma-Aguilar, Superconfinement tailors fluid flow at microscales, Nature communications 6. doi:10.1038/ncomms8297.

[48] A. Demianov, O. Dinariev, N. Evseev, Density functional modelling in multiphase compositional hydrodynamics, The Canadian Journal of Chemical Engineering 89 (2) (2011) 206–226. doi:10.1002/cjce.20457.

[49] D. Jacqmin, Contact-line dynamics of a diffuse fluid interface, Journal of Fluid Mechanics 402 (2000) 57–88. doi:10.1017/S0022112099006874.

[50] P. Seppecher, Moving contact lines in the Cahn-Hilliard theory, International Journal of Engineering Science 34 (9) (1996) 977 – 992. doi:10.1016/0020-7225(95)00141-7.

[51] A. J. Briant, A. J. Wagner, J. M. Yeomans, Lattice boltzmann simulations of contact line motion. i. liquid-gas systems, Phys. Rev. E 69 (3) (2004) 031602. doi:10.1103/PhysRevE.69.031602.

[52] A. J. Briant, J. M. Yeomans, Lattice Boltzmann simulations of contact line motion. II. Binary fluids, Phys. Rev. E 69 (3) (2004) 031603. doi:10.1103/PhysRevE.69.031603.

[53] P. G. de Gennes, Wetting: statics and dynamics, Rev. Mod. Phys. 57 (3) (1985) 827–863. doi:10.1103/RevModPhys.57.827.

[54] V. Kendon, M. Cates, I. Pagonabarraga, J.-C. Desplat, P. Bladon, Inertial effects in three-dimensional spinodal decomposition of a symmetric binary fluid mixture: a lattice boltzmann study, Journal of Fluid Mechanics 440 (2001) 147–203. doi:10.1017/S0022112001004682.

[55] J. Cahn, Critical-Point Wetting, J. Chem. Phys. 66 (1977) 3367. doi:10.1063/1.434402.

[56] D. M. Anderson, G. B. McFadden, A. A. Wheeler, Diffuse-interface methods in fluid mechanics, Annual Review of Fluid Mechanics 30 (1) (1998) 139–165. doi:10.1146/annurev.fluid.30.1.139.

[57] Q. Li, A. J. Wagner, Symmetric free-energy-based multicomponent lattice Boltzmann method, Phys. Rev. E 76 (2007) 036701. doi:10.1103/PhysRevE.76.036701.

[58] J. Zhang, D. Y. Kwok, A mean-field free energy lattice Boltzmann model for multicomponent fluids, The European Physical Journal Special Topics 171 (1) (2009) 45–53. doi:10.1140/epjst/e2009-01010-2.

[59] D. D'Humières, I. Ginzburg, M. Krafczyk, P. Lallemand, L.-S. Luo, Multiple-relaxation-time lattice Boltzmann models in three dimensions, Royal Society of London Philosophical Transactions Series A 360 (2002) 437. doi:10.1098/rsta.2001.0955.

[60] R. G. Cox, The dynamics of the spreading of liquids on a solid surface. Part 1. Viscous flow, Journal of Fluid Mechanics 168 (1986) 169–194. doi:10.1017/S0022112086000332.

[61] P. Sheng, M. Zhou, Immiscible-fluid displacement: Contact-line dynamics and the velocity-dependent capillary pressure, Physical Review A 45 (8) (1992) 5694. doi:10.1103/PhysRevA.45.5694.

[62] M. Latva-Kokko, D. H. Rothman, Scaling of dynamic contact angles in a lattice-Boltzmann model, Phys. Rev. Lett. 98 (25) (2007) 254503. doi:10.1103/PhysRevLett.98.254503.

[63] S. Seth, N. R. Morrow, Efficiency of the conversion of work of drainage to surface energy for sandstone and carbonate, SPE Reservoir Evaluation & Engineering 10 (04) (2007) 338–347. doi:10.2118/102490-PA.

[64] J. Niessner, S. Berg, S. Hassanizadeh, Comparison of Two-Phase Darcy's Law with a Thermodynamically Consistent Approach, Transport in Porous Media 88 (1) (2011) 133–148. doi:10.1007/s11242-011-9730-0.

[65] P. A. Gauglitz, C. J. Radke, Dynamics of Haines jumps for compressible bubbles in constricted capillaries, AIChE Journal 35 (2) (1989) 230–240. doi:10.1002/aic.690350207.

[66] L. C. Nielsen, I. C. Bourg, G. Sposito, Predicting CO2water interfacial tension under pressure and temperature conditions of geologic {CO2} storage , Geochimica et Cosmochimica Acta 81 (2012) 28 – 38. doi:10.1016/j.gca.2011.12.018.

[67] H. E. Huppert, J. A. Neufeld, The fluid mechanics of carbon dioxide sequestration, Annual Review of Fluid Mechanics 46 (1) (2014) 255–272. doi:10.1146/annurev-fluid-011212-140627.